AIAA JOURNAL
Vol. 47, No. 12, December 2009

Large-Eddy Simulation of Swirling Turbulent Jet Flows in Absence of Vortex Breakdown

Celestin P. Zemtsop,* Michael K. Stöllinger,* Stefan Heinz,† and Dan Stanescu*
University of Wyoming, Laramie, Wyoming 82071

DOI: 10.2514/1.43813

This paper reports the results of numerical investigations of swirling turbulent jet flows by large-eddy simulation. Reynolds-averaged Navier–Stokes simulations are used to generate mean inflow data. Fluctuations are added to the profiles of the means to produce instantaneous inflow data. The instantaneous inflow data are correlated such that the characteristic length and time scales of inflowing turbulent eddies are consistent with the corresponding Reynolds-averaged Navier–Stokes profiles imposed at the inlet. The resulting large-eddy simulation method is validated against experimental data of both swirling and nonswirling turbulent jets. The application of the validated large-eddy simulation method to studies of the mechanism of swirl effects shows the following. Swirl breaks apart the typical ring structures of nonswirling turbulent jets into two modes: a helical mode and streamwise braid structures. The interaction of these two modes generates unorganized turbulence that enhances the turbulent mixing. An analysis of the mixing enhancement by swirl shows a significant increase of the turbulent mixing efficiency of scalars with the swirl number (of up to 21.7% for the cases considered).

Nomenclature

a_{ij}	=	matrix formed by eigenvectors of the Reynolds stress σ_{ij} $(i, j = 1, 3)$
C_k	=	dynamic kinetic energy model stress model parameter
C_s	=	Smagorinsky constant
c_k	=	forcing model parameters $(k = 1, 3)$, see Eq. (7)
D	=	nozzle exit diameter
D_0	=	nozzle inlet diameter
I	=	intensity of segregation, $I = \sigma_\phi^2/[\Phi(1-\Phi)]$
k	=	turbulent kinetic energy
k_i^n	=	random numbers $(i, n = 1, 3)$, $k_i^n \in N(0, \frac{1}{2})$
k_{sgs}	=	subgrid-scale kinetic energy
k_0	=	normalization variable for k, U_0^2
L	=	length scale of turbulence, $k^{1/2}\tau$
m_e	=	mixing efficiency, $1 - I$
N	=	number of Fourier modes, see Eq. (8)
$N(m, s)$	=	normal distribution with mean m and standard deviation s
P	=	mean pressure
p	=	instantaneous pressure
$\langle q \rangle$	=	ensemble average of any variable q
$\bar{q}$	=	filtered value of any variable q
R	=	nozzle exit radius, $D/2$
Re	=	Reynolds number based on the averaged nozzle exit axial velocity and D
rms q	=	root mean square of any variable q
S	=	swirl number, see Eq. (1)
Sc	=	Schmidt number, 1
Sc_t	=	turbulent Schmidt number, 1
S_{ij}	=	instantaneous rate-of-strain tensor $(i, j = 1, 3)$, $[\partial u_i/\partial x_j + \partial u_j/\partial x_i]/2$
S_1	=	swirl number, see Eq. (2)
S_2	=	swirl number, see Eq. (3)
$\lvert\bar{S}\rvert$	=	characteristic large-eddy simulation strain rate, $(2\bar{S}_{ij}\bar{S}_{ij})^{1/2}$
t	=	time
t_e	=	eddy turnover time, D/U_0
U, W	=	mean axial and tangential velocity components, respectively
U_0, W_0	=	maximum axial and tangential velocities at the nozzle exit, respectively
u, v, w	=	Reynolds-averaged Navier–Stokes velocity fluctuations of axial, radial, and azimuthal velocity components, respectively
u_i	=	instantaneous velocity components $(i = 1, 3)$
v_k	=	flowfield vector $(k = 1, 3)$, see Eq. (8)
x, r, θ	=	cylindrical coordinate system: axial, radial, and angular coordinates, respectively
x_i	=	Cartesian coordinate system $(i = 1, 3)$
Δ	=	filter width
ϵ	=	dissipation rate of turbulent kinetic energy k
ϵ_{ijk}	=	permutation tensor $(i, j, k = 1, 3)$
ζ_i^n	=	random numbers, $\zeta_i^n \in N(0, 1)$
ν	=	kinematic viscosity
ν_T	=	Reynolds-averaged Navier–Stokes turbulent viscosity
ν_t	=	subgrid-scale viscosity
ξ_i^n	=	random numbers, $\xi_i^n \in N(0, 1)$
ρ	=	fluid mass density, 0.9 kg/m^3
σ_{ij}	=	Reynolds stress tensor $(i, j = 1, 3)$
σ_ϕ^2	=	variance of ϕ, $\langle(\phi - \Phi)^2\rangle$
τ	=	time scale of turbulence, $\tau = k/\epsilon$
Φ	=	mean passive scalar
ϕ	=	instantaneous passive scalar
ω	=	turbulence frequency, $1/\tau$
ω^n	=	random numbers, $\omega^n \in N(0, 1)$

I. Introduction

IMPROVING the efficiency of turbulent jet mixing can produce several performance enhancements for aircraft, including decreased jet noise, lower plume temperatures, increased combustion efficiency, and reduced pollutant emission. One proven mixing enhancement approach is the use of swirl, which is known to enhance jet growth rates due to changes in the jet turbulence [1,2]. Swirl is also used to improve the turbulent mixing in many other flows. In nonreacting cases, applications include cyclone separators, spraying systems, and jet pumps. In combustion systems, swirling

Received 13 February 2009; revision received 30 July 2009; accepted for publication 1 August 2009.

*Department of Mathematics, 1000 East University Avenue.
†Department of Mathematics, 1000 East University Avenue; heinz@uwyo.edu.

jets are used as means of controlling flames: swirl helps to increase the burning intensity through enhanced mixing and a higher residence time. Swirl is applied in systems such as gas turbines, utility boilers, industrial furnaces, internal combustion engines, and many other practical heating devices [3]. In previous studies [4–7], it was found that swirling turbulent jets are affected by several types of coherent structures (ring structures, braids, helical structures). The analysis of dynamics of these coherent structures turns out to be very difficult, and the results may depend on the flow considered. Thus, the modifications of these coherent structures (the underlying mechanisms of mixing enhancement) by swirl is not well understood at present.

Investigations of swirl effects by experiments and numerical simulations are very challenging. Experimental studies may provide insight into the spatial changes of mean flow and turbulence characteristics [2,8–10]. However, information about characteristic length and time scales of turbulent motions and insight into the temporal dynamics of coherent structures are difficult to obtain in this way. Numerical simulations can provide insight into the mechanism of swirling turbulent jets. Reynolds-averaged Navier–Stokes (RANS) methods represent the most efficient methodology for the calculation of turbulent flows, but the use of standard RANS methods for swirling jet flow simulations has, to date, turned out to be inappropriate [11]. Large-eddy simulation (LES) has proven to be an accurate and computationally feasible approach for turbulent swirl flow simulations [4–7]. However, there are also questions regarding the realization of such LES. The inflow conditions of jet flows are often determined by a nozzle flow, which has a significant influence on the jet flow development. Experimental studies of flowfields at a nozzle exit often provide limited information about inflow data for LES. For example, the dissipation rate of turbulent kinetic energy that provides information about the typical length and time scales of inflowing eddies is usually missing. Unfortunately, LES of the nozzle flow is often infeasible: the simulation of near-wall fluid motions requires computational costs that are comparable with those of direct numerical simulation [12,13]. Thus, nozzle flow simulations have to be performed on the basis of RANS simulations. This approach involves the need for a forcing that generates instantaneous inflow data. However, the optimal generation of such a forcing is still unclear [4,14–16].

The questions discussed previously will be addressed here by a computational study of swirling turbulent jet flows. Gilchrist and Naughton's [17] experimental data for a nonswirling jet and a jet with a mild swirl (swirl number $S = 0.23$) are used to investigate the suitability of an LES code. This evaluation of LES results is performed by comparing measured data of averaged variables with corresponding time-averaged LES data. The LES code validated in this way is used to study the characteristics of a variety of swirling jet flows with swirl numbers ranging from zero to one. The LES data are then used for the analysis of instantaneous velocity and passive scalar fields. The goal of this analysis is to study the dynamics of coherent structures and the swirl-induced mixing enhancement.

The paper is organized in the following way. The flows considered will be described in Sec. II. Sections III and IV describe the generation of LES inflow data. The realization of LES is described in Sec. V, and a comparison of averaged LES results with available experimental data is provided in Sec. VI. In particular, these comparisons are used to evaluate the relevance of the forcing applied and the suitability of several subgrid-scale (SGS) stress models. Sections VII and VIII deal with an investigation of instantaneous LES data: swirl effects on the velocity field and the mixing of a passive scalar will be discussed. Finally, Sec. IX summarizes the results reported here.

II. Experimental Data

The flows considered are Gilchrist and Naughton's [17] swirling turbulent jet flows. The nozzle and jet flows considered are illustrated in Fig. 1. Gilchrist and Naughton used a unique facility that allowed for fine control of the tangential velocity profile and the creation of a swirling jet that was largely free from artifacts produced by the swirl generation process. Two swirl profiles have been investigated in these experiments: one resembling a q vortex (solid-body core with a free vortex outer region) and the other resembling a solid-body rotation. However, the mean fields and turbulence characteristics of both swirl profile cases were about the same [17]. Thus, only the solid-body rotation cases will be considered here. The Reynolds number Re was $Re = 1.0 \times 10^5$ for all cases considered. This value was based on the nozzle diameter $D = 0.0381$ m and the value 50 m/s of the nozzle exit axial velocity averaged over its radial profile. Experimental data of mean variables and turbulence statistics [17] were available for the nonswirling case $S = 0$ and the case $S = 0.23$ of mild swirl. Here, the swirl number S at the nozzle exit plane ($x = 0$) was defined by the ratio of angular momentum flux to the flux of linear momentum [8]

$$S = \left\{\int_0^R r^2[UW + \langle uw\rangle]\,\mathrm{d}r\right\} \Big/ \left\{R\int_0^R r[U^2 - W^2/2 + \langle uu\rangle - (\langle vv\rangle + \langle ww\rangle)/2]\,\mathrm{d}r\right\} \tag{1}$$

Here, U was the mean axial velocity component, W was the mean tangential velocity component, r was the radial position, and $R = D/2$. The Reynolds stresses involved were the normal stress in the axial direction $\langle uu\rangle$, the normal stress in the radial direction $\langle vv\rangle$, the normal stress in the tangential direction $\langle ww\rangle$, and the shear stress in the tangential direction $\langle uw\rangle$.

It is worth noting that the definition (1) of the swirl number applied here is one choice out of a variety of swirl numbers in use [18]. A second possible definition is given, for example, by neglecting the influence of turbulence in Eq. (1) [19]:

$$S_1 = \left\{\int_0^R r^2 UW\,\mathrm{d}r\right\} \Big/ \left\{R\int_0^R r[U^2 - W^2/2]\,\mathrm{d}r\right\} \tag{2}$$

and a third possibility is given by [18,20]:

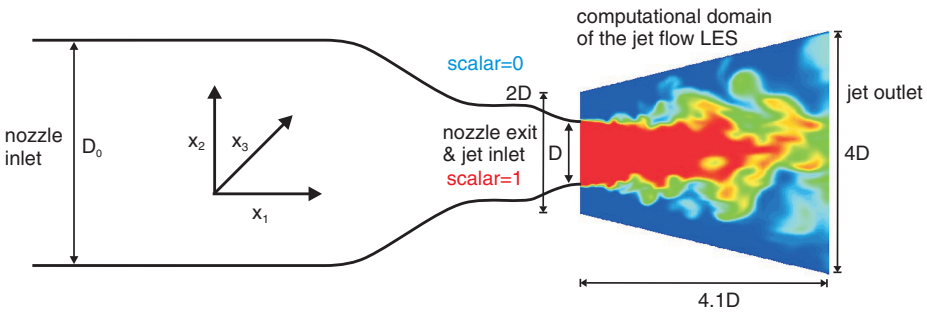

Fig. 1 Nozzle design and computational domain for the jet LES. The nozzle is shown schematically on the left-hand side. $D_0 = 0.248$ m is the nozzle diameter at the inlet, and $D = 0.0381$ m is the nozzle diameter at the exit. The nozzle length is $11.65D$. The Cartesian coordinate system applied is also shown. The computational domain for the jet LES on the right-hand side is a conical domain with diameters of $2D$ and $4D$, respectively. The domain length is $4.1D$.

$$S_2 = \left\{ \int_0^R r^2 UW \, \mathrm{d}r \right\} \Big/ \left\{ R \int_0^R rU^2 \, \mathrm{d}r \right\} \tag{3}$$

It is relevant to note that there is actually no difference between the swirl numbers S and S_1 for the flows considered. The magnitude of the relative error of the simplified version (2) compared with Eq. (1) is less than 0.13%; this means the effect of turbulence on the definition of the swirl number is negligible for the flows considered. Regarding the use of Eq. (3), it turns out that there is a difference between S and S_2 caused by the neglect of the squared tangential velocity. For $0 \leq S \leq 1$, S and S_2 are related by

$$S_2 = \left[\frac{3.9S}{1 + 4.1S} \right]^2 \tag{4}$$

The magnitude of the relative error of the latter approximation is less than 2%.

The experiments of Gilchrist and Naughton [17] revealed a significant effect of swirl numbers S greater than 0.1 on the jet momentum half-width. Unfortunately, these investigations did not identify the mechanism behind the enhanced growth rates and the related modifications of the turbulence structures. Such insight was relevant to the use of swirl for optimizing the enhancement of turbulent mixing in technical applications as well as providing further understanding of a canonical turbulent flow. This question could be addressed by LES of swirling jet flows as shown in the following.

III. Mean Large-Eddy Simulation Inflow

Jet inflow data are required to simulate the flows described in Sec. II. As explained previously, the most appropriate way to provide profiles of mean variables at the nozzle exit (the jet inflow plane) is given by RANS simulations of the nozzle flow. Such RANS simulations will be described next.

The RANS equations for incompressible flows are given by the conservation of mass equation:

$$\frac{\partial \langle u_i \rangle}{\partial x_i} = 0 \tag{5}$$

and the conservation of momentum equation

$$\frac{\partial \langle u_i \rangle}{\partial t} + \frac{\partial \langle u_i \rangle \langle u_j \rangle}{\partial x_j} = -\frac{\partial (\langle p \rangle / \rho + 2k/3)}{\partial x_i} + 2 \frac{\partial (\nu + \nu_T) \langle S_{ij} \rangle}{\partial x_j} \tag{6}$$

for which an eddy viscosity model for the Reynolds stress is applied. Here, x_i refers to the position in space and t is time. The components of the instantaneous velocity field are denoted by u_i, p is the instantaneous pressure, and $S_{ij} = [\partial u_i / \partial x_j + \partial u_j / \partial x_i]/2$ is the instantaneous rate-of-strain tensor. The sum convention is used throughout this paper for repeated subscripts. The symbol $\langle q \rangle$ denotes the ensemble average of any variable q. The fluid density ρ is constant. The kinematic viscosity is ν, and k is the turbulent kinetic energy. Equation (6) is unclosed as long as the turbulent viscosity ν_T is not defined. Several standard turbulence models for the closure of ν_T are applied to perform RANS simulations of the nozzle flow. However, only the shear stress transport (SST) $k - \omega$ model [21] provides acceptable results. In this model, the turbulent viscosity is a function of the turbulent kinetic energy k and the turbulence frequency ω. Transport equations suggested by Menter [21] govern k and ω.

The RANS Eqs. (5) and (6) closed in this way required boundary conditions. A constant axial velocity at the nozzle inlet was calculated in the following way. The conservation of mass required that the mass flow rate through the nozzle was constant. Correspondingly, the axial velocity at the nozzle inlet was calculated by setting the mass flow rate at the nozzle inlet, equal to the known mass flow rate at the nozzle exit. In this way, the axial velocity values 1.05 m/s ($S = 0$) and 1.17 m/s ($S = 0.23$) were found. A profile for the tangential velocity at the nozzle inlet was calculated on the basis of the conservation of angular momentum. In particular, the parameters of a piecewise linear tangential velocity profile were adjusted, such that the angular momentum at the nozzle inlet was equal to the angular momentum at the nozzle exit. The radial profile of the tangential velocity obtained in this way for the $S = 0.23$ case is shown in Fig. 2. The corresponding tangential velocity profiles for the other swirl cases considered (see Sec. VII) were obtained by a rescaling of the $S = 0.23$ profile: the latter was multiplied with 2.25, 4.2, and 6.8 for the $S = (0.5, 0.75, 1)$ cases, respectively. The settings for axial and tangential velocities were combined with a zero radial velocity at the nozzle inlet. The flow was almost laminar at the nozzle inlet. Correspondingly, k was calculated by assuming a turbulence intensity of 0.01%. The characteristic turbulence length scale L was calculated by $L = 0.07D_0$, where D_0 referred to the nozzle inlet diameter. The latter assumption was known to represent a reasonable approximation for pipe flow [22,23]. The combination of the definition $L = k^{1/2}/\omega = k^{3/2}/\epsilon$ with $L = 0.07D_0$ enabled the calculation of ω and ϵ by $\omega = k^{1/2}/(0.07D_0)$ and $\epsilon = k^{3/2}/(0.07D_0)$. The reason for assuming a nonzero turbulence intensity of 0.01% was to keep the turbulent viscosity ν_T (which was proportional to k/ω) finite. It was proven that variations of the turbulence intensity ranging from 0.01 to 1% led to changes of maximum velocity and turbulent kinetic energy values at the nozzle exit that were smaller than 0.1%. A no-slip boundary condition was used for the velocity at the wall. At the nozzle outlet, the pressure was set equal to the atmospheric pressure, and zero-gradient boundary conditions were used for the velocity, the turbulent kinetic energy k, and the turbulence frequency ω.

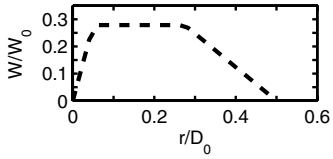

Fig. 2 The swirl number $S = 0.23$ solid-body case (the nozzle inlet profile of the normalized tangential velocity W). The normalization data are $W_0 = 21.7$ m/s and $D_0 = 0.248$ m.

The computational domain is shown in Fig. 1. The number of grid points applied was 78,000. A boundary layer mesh with a stretching of 12% was used to improve the resolution of near-wall fluid flow. All simulations have been performed with the computational fluid dynamics (CFD) package FLUENT [22]. The equations were solved on a two-dimensional axisymmetric domain using the finite volume method. A second-order upwind scheme was used for the spatial discretization of the equations for the momentum, turbulent kinetic energy k, and turbulence frequency ω. The SIMPLEC method (semi-implicit method for pressure-linked equations consistent) was used for the pressure–velocity coupling. The numerical settings are given in Table 1.

Simulation results of the $S = 0$ and $S = 0.23$ swirl cases are shown in Fig. 3. In the nonswirling flow, the tangential velocity is zero, and k is one order of magnitude smaller than the turbulent kinetic energy values of the $S = 0.23$ case. No experimental data are available regarding the turbulent dissipation rate ϵ. Therefore, only the normalized axial velocity U/U_0 for the $S = 0$ and $S = 0.23$ cases, and the normalized tangential velocity W/W_0 and normalized

Table 1 Numerical setup for the RANS simulation of nozzle flows

Simulations tools	Settings
Domain	Axisymmetric, the domain geometry is shown in Fig. 1
Method	Finite volume
Discretization	Second-order upwind for momentum, k, and ω
Discretization	Pressure staggering option (PRESTO) for pressure
Discretization	SIMPLEC for pressure–velocity coupling
Discretization	Steady state
Turbulence model	The SST $k - \omega$ model [21] with constants $\sigma_{k,1} = 1.176$, $\sigma_{\omega,1} = 2$, $\sigma_{\omega,2} = 1.168$, $a_1 = 0.31$, $\beta_{i,1} = 0.075$, and $\beta_{i,2} = 0.0828$

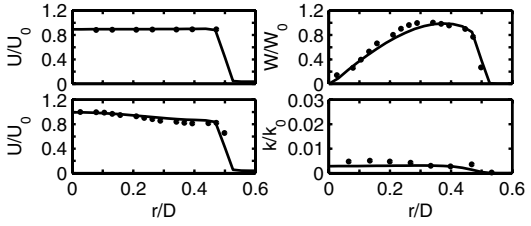

Fig. 3 Radial distributions of the mean axial velocity U for the nonswirling $S = 0$ case (upper left) and for the $S = 0.23$ swirl case (lower left), the tangential velocity W and turbulent kinetic energy k for the $S = 0.23$ swirl case at $x/D = 0$. The solid lines denote RANS simulations and the dots denote experimental data from Gilchrist and Naughton [17]. The normalization data are the maximum values of the velocity profiles: $U_0 = 50.4$ m/s for the nonswirling flow, $U_0 = 56.3$ m/s for the swirling flow, and $W_0 = 21.7$ m/s. In addition, the values $k_0 = U_0^2$ and $D = 0.0381$ m are applied.

turbulent kinetic energy k/k_0 for the $S = 0.23$ case are shown in Fig. 3. The axial and tangential velocities and the turbulent kinetic energy agree well with the measurements: the global average errors (the mean values of the relative errors of computations in comparison to measured data) of the simulated axial velocity, the tangential velocity, and the turbulent kinetic energy are 2.7, 5.2, and 7.8%, respectively. The validity of the dissipation rate profiles obtained by the RANS simulations is supported by the good agreement of the velocities and turbulent kinetic energy with the experimental data. The overall agreement of the RANS simulation results with the available experimental data at the nozzle exit support the results of RANS simulations.

IV. Instantaneous Large-Eddy Simulation Inflow

The importance of specifying instantaneous inflow conditions for LES is very well known [15,16,24]. Thus, this section addresses the question of how fluctuating velocities at the jet inlet can be generated by adding fluctuating velocity components to the mean velocities obtained by RANS simulations.

The random flow generation (RFG) technique of Smirnov et al. [14] is used to generate fluctuating velocities. This flowfield generation technique is based on the RFG technique originally proposed by Kraichnan [25]. In this method, fluctuating velocities are computed by scaling a divergence-free velocity vector field $v_i(\mathbf{x}, t)$ obtained from the summation of Fourier harmonics. In particular, instantaneous velocity components are defined by

$$u_i = \langle u_i \rangle + a_{ik} c_k v_k \tag{7}$$

Here, a_{ij} is the matrix formed by the eigenvectors of the Reynolds stress tensor σ_{ij} that is calculated by the RANS simulation of the nozzle flows. The square roots of the absolute values of eigenvalues of eigenvectors that form the matrix a_{ij} are c_k. The sum convention also applies to the three repeated subscripts k in Eq. (7). The three-dimensional flowfield vector $v_i(\mathbf{x}, t)$ is defined by

$$v_i(\mathbf{x}, t) = \sqrt{\frac{2}{N}} \sum_{i=1}^{N} \epsilon_{ilm} \left[\zeta_l^n k_m^n \cos\left(\frac{k_j^n x_j}{\tau c_j} + \frac{\omega^n t}{\tau} \right) + \xi_l^n k_m^n \sin\left(\frac{k_j^n x_j}{\tau c_j} + \frac{\omega^n t}{\tau} \right) \right] \tag{8}$$

$N = 1000$ is the number of Fourier modes [14] and ϵ_{ijk} is the permutation tensor. The random numbers are ζ_l^n, ξ_l^n, ω^n, and k_j^n:

$$\zeta_l^n,\ \xi_l^n,\ \omega^n \in N(0,\ 1), \qquad k_j^n \in N(0,\ \tfrac{1}{2})$$

where $N(m, s)$ is a normal distribution with mean m and standard deviation s. The time scale of turbulence that is available from the RANS simulations of the nozzle flow is $\tau = k/\epsilon$. The advantage of this RFG technique is given by the generation of correlated noise [24,26] that results in characteristic length and time scales of inflowing instantaneous turbulent eddies that are consistent with the corresponding RANS profiles imposed at the inlet.

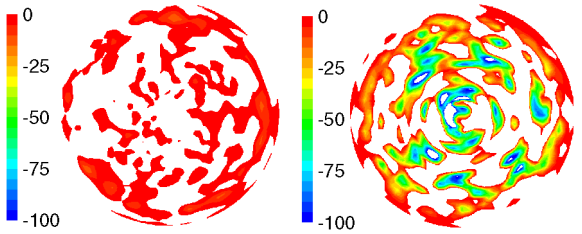

Fig. 4 Contour plots of pressure fluctuations $\bar{p} - P$ in Pa for the $S = 0$ (left) and $S = 0.23$ (right) forced LES at the first grid points of the computational domain.

Figure 4 illustrates the suitability of the forcing described in the preceding paragraph. This figure shows contour plots of pressure fluctuations at the first grid points of the computational domain for swirling and nonswirling jet flows. It is worth noting that the pressure fluctuations shown are not obtained by the RFG method of Smirnov et al. [14], but they are the result of simulations. The pressure inside a vortex is low compared with its surroundings [4]. Thus, contour plots of pressure fluctuations can be used to identify turbulent eddies. Figure 4 shows that the RFG method applied generates turbulent eddies. The eddies are relatively small in the nonswirling flow compared with the swirling flow. This observation can be explained by the fact that the turbulence quantities in the nonswirling flow were found to be one order of magnitude smaller than the turbulence quantities in the swirling flow at the jet inlet. In addition, integral length and time scales calculated by the RFG technique were compared with the characteristic length scale $L = k^{1/2}\tau$ and time scale τ of the turbulent eddies provided by the RANS method. A discrepancy of only 15% was found. The latter result supports the view that the turbulent eddies are well represented by the RFG method.

V. Jet Flow Large-Eddy Simulation

A box filtering was applied for the derivation of LES equations [27]. By adopting eddy diffusivity models for the SGS stress and turbulent scalar flux, the incompressible LES equations for filtered velocities $\bar{u}_i$ $(i = 1, 3)$ and a passive scalar $\bar{\phi}$ are given by

$$\frac{\partial \bar{u}_i}{\partial x_i} = 0 \tag{9}$$

$$\frac{\partial \bar{u}_i}{\partial t} + \frac{\partial \bar{u}_i \bar{u}_j}{\partial x_j} = -\frac{\partial(\bar{p}/\rho + 2k_{\text{sgs}}/3)}{\partial x_i} + 2\frac{\partial(\nu + \nu_t)\bar{S}_{ij}}{\partial x_j} \tag{10}$$

$$\frac{\partial \bar{\phi}}{\partial t} + \bar{u}_j \frac{\partial \bar{\phi}}{\partial x_j} = \frac{\partial}{\partial x_j}\left(\frac{\nu}{Sc} + \frac{\nu_t}{Sc_t} \right) \frac{\partial \bar{\phi}}{\partial x_j} \tag{11}$$

Here, $\bar{p}$ is the filtered pressure, ρ is the constant fluid mass density, and $\bar{S}_{ij}$ is the filtered rate-of-strain tensor. The kinematic viscosity is referred to again by ν, and k_{sgs} is the SGS kinetic energy. The Schmidt number Sc and the turbulent Schmidt number Sc_t are given by $Sc = Sc_t = 1$.

Three models for the SGS viscosity ν_t are considered here: the standard Smagorinsky model (SSM) [28], the dynamic Smagorinsky model (DSM) [29], and the dynamic kinetic energy model (DKEM) [30]. In the SSM, the eddy viscosity is modeled by

$$\nu_t = (C_s \Delta)^2 |\bar{S}| \tag{12}$$

Here, C_s is the Smagorinsky constant, Δ is the filter width, and $|\bar{S}| = (2\bar{S}_{ij}\bar{S}_{ij})^{1/2}$. In the DSM, expression (12) is also used for the SGS viscosity ν_t, but C_s is dynamically computed. In the DKEM, the SGS viscosity ν_t is calculated by

Table 2 Numerical setup for the LES jet flows

Simulations tools	Settings
Domain	Three-dimensional: conic with length $4.1D$, radius $1D$, and $2D$ (divided into 370, 000 cells).
Method	Finite volume
Discretization	Bounded central differencing for momentum [22]
Discretization	PRESTO for pressure
Discretization	SIMPLEC for pressure–velocity coupling, implicit second-order for time, $\Delta t = 5 \cdot 10^{-5}$ s
SGS models	DSM [29] with $0 \leq C_s \leq 0.23$
SGS models	SSM [28] with $C_s = 0.17$
SGS models	DKEM [30]

$$\nu_t = C_k k_{\text{sgs}}^{1/2} \Delta \tag{13}$$

Here, k_{sgs} was obtained by solving a transport equation, and the model parameter C_k was calculated dynamically [30]. The instantaneous inflow boundary condition was given by Eq. (7), involving the RANS velocity profile plus fluctuations generated by the RFG method. A pressure inlet boundary condition was used for far-field boundaries, and a pressure outlet boundary condition was used for the outlet boundary. The scalar is equal to one at the jet inlet and zero elsewhere at the inlet plane. The scalar value was set to zero at the far-field boundaries, and a zero-gradient boundary condition was applied at the outlet.

The computational domain was conical with a radius of $1D$ and $2D$ at the inlet and outlet, respectively. The domain extended up to $4.1D$ downstream. The domain was discretized into 80 points in an azimuthal direction (uniformly distributed), 60 points in a radial direction (uniformly distributed), and 80 points in an axial direction with a stretching of 2%. The effects of a grid refinement and a variation of the domain size are reported next (see the first paragraphs of Secs. VI and VII , respectively). The incompressible LES equations have been solved by a finite volume method based on the CFD code FLUENT [22]. Bounded central differencing was used for the spatial discretization of the momentum equations, a second-order upwind scheme was used for the spatial discretization of the passive scalar equation, and time was advanced via a second-order-accurate implicit scheme. The SIMPLEC method was used for the pressure–velocity coupling. Details of the numerical setup are summarized in Table 2.

McIlwain and Pollard [4] have studied similar flows. Their simulations were run for 12 large-eddy turnover times $t_e = D/U_0$ to eliminate the effects of initial conditions. Our simulations were run for 15 t_e to eliminate the effects of the initial conditions. This approach was justified by monitoring time statistics that reached a steady state in less than 15 large-eddy turnover times in all the simulations. After this time, the simulations were run for another 920 large-eddy turnover times to collect time statistics. Samples were taken every fifth time step, giving a total of 2500 samples. Because of the axisymmetry of the flow, an additional averaging of the time statistics over 80 points in the azimuthal direction had been performed. All averages referred to in this paper have been obtained by this method. All the simulations have been performed on 12 processors of a Beowulf Linux cluster provided and operated by the Institute for Scientific Computation at the University of Wyoming. Obtaining the necessary time statistics required a computational time of about 72 h.

VI. Jet Flow Large-Eddy Simulation Evaluation

The grid dependence of LES calculations was investigated by adopting a finer grid for LES simulations of the swirling jet flow with $S = 0.23$. The domain size was the same as described in Sec. V, but the computational domain was now discretized into 112 points in an azimuthal direction (uniformly distributed), 84 points in a radial direction (uniformly distributed), and 112 points in an axial direction with a stretching of 1%. Simulation results for the grid, described in Sec. V, and the finer grid LES are shown in Fig. 5. The DSM was used for the SGS stress closure. Figure 5 shows the rms u/U_0 and the rms w/W_0 of axial and azimuthal velocity fluctuations, respectively (the abbreviation rms refers to the root mean square of the variable considered). This figure indicated a very small grid dependence of LES results. The grid dependence is quantified in terms of Fig. 6, which shows the axial distribution of the resolved turbulent kinetic energy k along a line offcenter ($r = 0.5D$) for the swirling case $S = 0.23$. The corresponding Error $= 100(k_{\text{fine}} - k_{\text{coarse}})/k_{\text{coarse}}$ is also shown, where k_{fine} and k_{coarse} refer to the calculations of k with the fine and coarse grid, respectively. The turbulent kinetic energy profiles show a very minor difference. In the region $0 < x/D < 1$, the error profile shows a peak of -46%. This peak is caused by very small values of k/k_0: $k_{\text{fine}}/k_0 = 0.0013$ and $k_{\text{coarse}}/k_0 = 0.0024$ at the peak position. The error oscillates between -3 and 6% for $1 < x/D < 4$. The last peak of 13.7% is likely caused by the boundary conditions. The overall feature that can be seen is that the error shows oscillations about zero of less than 6%, with the exception of regions close to the nozzle exit and the outflow boundary. This finding leads to the conclusion that the grid described in Sec. V is acceptable. Thus, the latter grid is used for all the calculations shown in the following.

The effect of the forcing, described in Sec. IV, was investigated by comparing averaged flow variables with experimental data [17] for the $S = 0$ and $S = 0.23$ cases. The DSM was used for the closure of the SGS stress. Simulation results for the forced LES and the unforced LES (for which the forcing was not applied) are shown in Figs. 7–10. In particular, Fig. 7 shows the radial distribution of the normalized averaged axial velocity U/U_0 and the normalized averaged azimuthal velocity W/W_0, Fig. 8 shows the intensity rms u/U_0 of axial velocity fluctuations, Fig. 9 shows the intensity rms w/W_0 of azimuthal velocity fluctuations, and Fig. 10 shows the

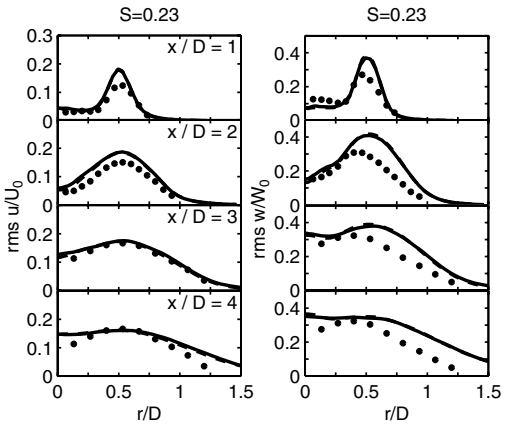

Fig. 5 Radial distributions of the normalized intensities rms u of axial velocity fluctuations and the normalized intensities rms w of azimuthal velocity fluctuations for the $S = 0.23$ case at different axial positions x/D. The DSM was applied to close the SGS stress. Solid lines refer to results obtained with the grid described in Sec. V, dashed lines refer to the finer grid described in Sec. VI, and dots denote the experimental data of Gilchrist and Naughton [17]. The normalization data are $U_0 = 56.3$ m/s and $W_0 = 21.7$ m/s.

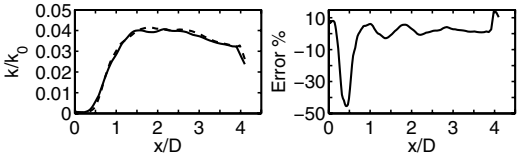

Fig. 6 The left-hand-side figure shows the axial distribution of the resolved turbulent kinetic energy k along a line $r = 0.5D$ for the swirling case $S = 0.23$. The solid line refers to the result obtained with the coarser grid, and the dashed line refers to the result obtained with the finer grid. The right-hand- side figure shows the corresponding Error$= 100(k_{\text{fine}} - k_{\text{coarse}})/k_{\text{coarse}}$, where k_{fine} and k_{coarse} refer to calculations of k with the fine and coarse grid, respectively.

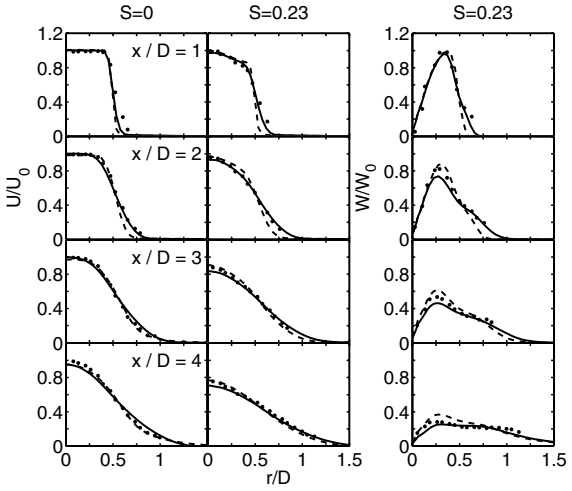

Fig. 7 Radial distributions of the normalized averaged axial velocity U and tangential velocity W for the cases $S = 0$ and $S = 0.23$ at different axial positions x/D. The DSM is applied to close the SGS stress. Solid lines refer to forced LES results, dashed lines refer to unforced LES results, and dots denote the experimental data of Gilchrist and Naughton [17]. The normalization data are $U_0 = 50.4$ m/s for the nonswirling case and $U_0 = 56.3$ m/s and $W_0 = 21.7$ m/s for the swirling case.

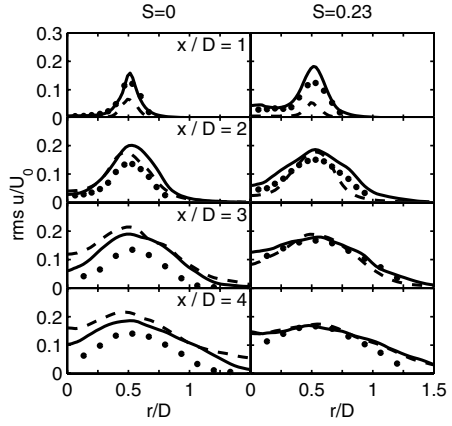

Fig. 8 Radial distributions of the normalized intensities rms u of axial velocity fluctuations for the cases $S = 0$ and $S = 0.23$ at different axial positions x/D. The DSM is applied to close the SGS stress. Solid lines refer to forced LES results, dashed lines refer to unforced LES results, and dots denote the experimental data of Gilchrist and Naughton [17]. The normalization data are $U_0 = 50.4$ m/s for the nonswirling case and $U_0 = 56.3$ m/s for the swirling case.

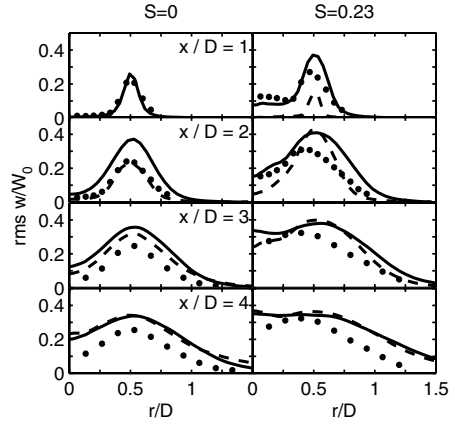

Fig. 9 Radial distributions of the normalized intensities rms w of azimuthal velocity fluctuations for the cases $S = 0$ and $S = 0.23$ at different axial positions x/D. The DSM is applied to close the SGS stress. Solid lines refer to forced LES results, dashed lines refer to unforced LES results, and dots denote the experimental data of Gilchrist and Naughton [17]. The normalization is given by $W_0 = 21.7$ m/s.

normalized averaged pressure P/P_0. The forced LES provides mean axial and azimuthal velocities that agree very well with the measurements. There is a minor overprediction of the intensities of axial and tangential velocity fluctuations. The calculated pressure agrees relatively well with the measured pressure: there is only a minor underprediction of the pressure minimum for $1 \leq x/D \leq 3$. The unforced LES results are different. The lack of forcing results in a significant underprediction of axial velocity fluctuations at $x/D = 1$. Hence, the jet expansion is underpredicted (see the corresponding axial velocity at $x/D = 1$). The latter implies steeper mean velocity gradients that generate more turbulence. Therefore, the intensity of axial velocity fluctuations increases strongly, which leads to the overprediction of axial velocity fluctuations observed at $x/D = 3$ and $x/D = 4$. The inclusion of forcing has, therefore, a positive effect regarding the cases considered.

The effect of different models for the SGS stress (the SSM, the DSM, and the DKEM) is shown in Figs. 11 and 12. These figures show the intensity of axial velocity fluctuations and the pressure for the forced $S = 0$ and $S = 0.23$ cases, respectively. Regarding the nonswirling case, the SSM significantly underpredicts the intensity of axial velocity fluctuations at $x/D = 1$. The SSM does not seem to capture the forcing applied at the inlet of the nonswirling jet flow. Overall, the SSM features are similar to the features of the unforced

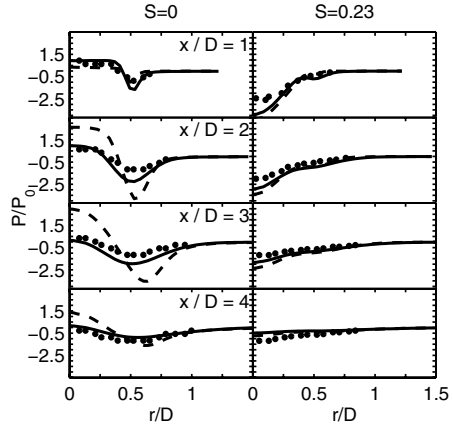

Fig. 10 Radial distributions of the normalized averaged pressure P for the cases $S = 0$ and $S = 0.23$ cases at different axial positions x/D. The DSM is applied to close the SGS stress. Solid lines refer to forced LES results, dashed lines refer to unforced LES results, and dots denote the experimental data of Gilchrist and Naughton [17]. The normalization data are $P_0 = 23$ Pa for the nonswirling case and $P_0 = 94$ Pa for the swirling case.

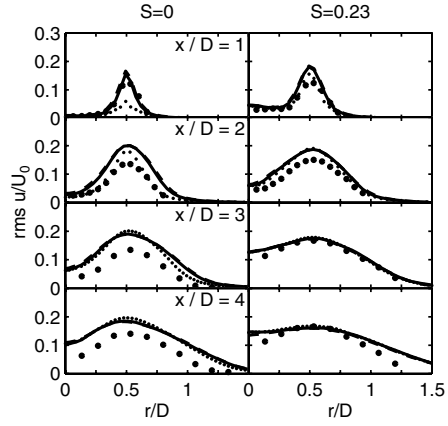

Fig. 11 Radial distributions of the normalized intensities rms u of axial velocity fluctuations for the forced cases $S = 0$ and $S = 0.23$ at different axial positions x/D. Solid lines refer to results obtained with the DSM, dashed lines refer to the DKEM results, smaller dots refer to the SSM results, and larger dots denote the experimental data of Gilchrist and Naughton [17]. Here, $U_0 = 50.4$ m/s for the nonswirling case and $U_0 = 56.3$ m/s for the swirling case.

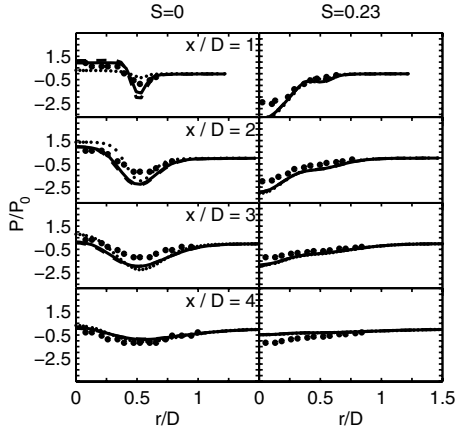

Fig. 12 Radial distributions of the normalized averaged pressure P for the forced cases $S = 0$ and $S = 0.23$ at different axial positions x/D. Solid lines refer to results obtained with the DSM, dashed lines refer to the DKEM results, little dots refer to the SSM results, and dots denote the experimental data of Gilchrist and Naughton [17]. The normalization data are $P_0 = 23$ Pa for the nonswirling case and $P_0 = 94$ Pa for the swirling case.

LES. For the swirling jet, the three SGS models considered predict almost the same flowfield. The features of the DSM and the DKEM are the same for both the swirling and nonswirling cases. Correspondingly, the SGS stress is closed by the DSM in all the simulations described in the next section.

VII. Swirl Effects

The validated LES code has been applied to simulations with higher swirl numbers to study the effect of swirl. The LES inlet profiles for these simulations were obtained as described in Sec. III. It turned out that vortex breakdown was observed for swirl numbers $S \geq 1.1$ (vortex breakdown was defined as an isolated axisymmetric recirculation zone which appears in the region downstream of a nozzle exit [31]). A comparison of this finding with experience obtained regarding the onset of vortex breakdown in other flows was very complicated. First, a variety of differently defined swirl numbers was applied in such studies (see Sec. II). In addition to this problem, the derivation of a general condition for the appearance of vortex breakdown seemed to be impossible. The critical swirl number at which the vortex breakdown occurred depended on the Reynolds number [32], and the critical swirl number was very sensitive to the inlet geometry and the outflow boundary condition [18]. By adopting a new computational domain long enough ($11.1D$ in the streamwise direction) to minimize the influence of the outflow boundary condition for the cases considered, it was checked that the observation about the onset of the vortex breakdown at $S = 1.1$ was unaffected by the boundary condition applied. The behavior of flows that involved the vortex breakdown was very different from the behavior of flows without the vortex breakdown. The natural first step of the investigations of the swirl effects was to explain the mechanism of swirl flows without the vortex breakdown. The latter is the objective of this paper, and so only swirl number cases with $S \leq 1$ were considered. In particular, simulations with swirl numbers $S = 0.5$, $S = 0.75$, and $S = 1$ were performed .

An analysis of instantaneous vorticity distributions was used recently by McIlwain and Pollard [4] to support the following idea of swirl effects. Ring structures aligned with the plane normal to the flow form downstream of the jet shear layer due to Kelvin–Helmholtz instabilities. The ring structures collided with the streamwise braid structures. The resulting interaction caused the ring to break apart into smaller, less organized turbulence structures. The addition of swirl increased the number of streamwise braids, which enhanced the breakdown mechanism of the rings. These observations suggested that the increased entrainment observed in the swirling flows was due to the action of the braids rather than the rings [4]. Instantaneous vorticity distributions were studied here in accordance with the analysis of McIlwain and Pollard [4]. It was found, however, that these fields did not represent an appropriate means to visualize coherent structures: the fields obtained did not reveal ring structures. The latter finding could be explained by the fact that McIlwain and Pollard's sinusoidal forcing was not applied here but the RFG forcing that generated correlated noise (see Sec. IV).

Thus, instantaneous pressure fluctuation fields, which are known to be appropriate to visualize coherent structures [6,7], are considered. Figure 13 shows an isosurface $\bar{p} - P = -20$ Pa of instantaneous pressure fluctuations for the nonswirling and swirling cases. The isosurface is colored in dependence on the filtered scalar

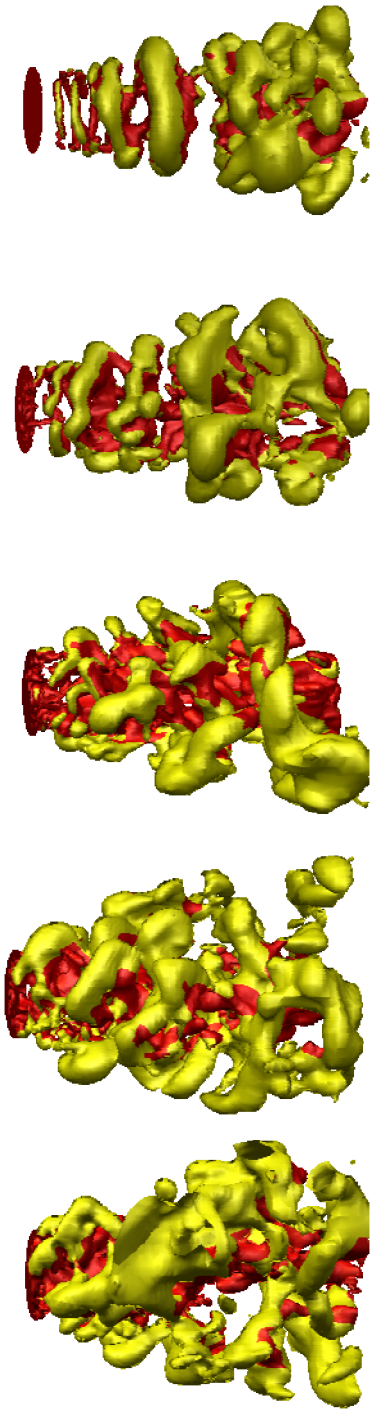

Fig. 13 Visualization of coherent vortex structures by means of an isosurface $\bar{p} - P = -20$ Pa of instantaneous pressure fluctuations for swirl number cases $S = 0$, 0.23, 0.5, 0.75, and 1 from the top to the bottom, respectively. The isosurface is colored according to the scalar value: $\tilde{\phi} \geq 0.5$ (darker areas) and $\tilde{\phi} < 0.5$ (lighter areas).

value. The $S = 0$ figure clearly reveals the existence of axisymmetric ring structures generated by Kelvin–Helmholtz instabilities, and streamwise braid structures are notably absent. The ring structures support the turbulent mixing (of a passive scalar, see the next section) only in part. In particular, this sort of coherent motion is well organized in the flow region close to the nozzle exit, which means that random structures which promote large-scale mixing do not appear in this flow region. The $S = 0.23$ figure shows a different flow behavior. In accordance with the conclusions of the linear instability theory [33], one can see that the axisymmetric ring structures are replaced by helical structures, and there are also streamwise braid structures observable in the flow region close to the nozzle exit. The resulting interaction between helical structures and streamwise braid structures causes the helical structures to break apart into smaller, less organized turbulence structures that enhance the turbulent mixing. The $S = 0.5$ figure shows an additional increase of the intensity of streamwise braid structures due to the increased swirl number. The streamwise braid structures are now capable of breaking apart the helical structures. The random motion of these pieces of the helical structures enhances the efficiency of turbulent mixing. A further increase of the swirl number (see the $S = 0.75$ and $S = 1$ cases) leads to the formation of larger-scale structures (the single pieces of the broken helical structures seem to merge). The random motion of these large-scale turbulence structures then leads to an additional increase of the efficiency of turbulent mixing. It is plausible to expect a maximum for this trend of merging structures after which the vortex breakdown is observed. This view of the mechanism of swirl effects is similar to McIlwain and Pollard's notion [4]. A difference is given by the observation of helical structures reported here. The latter observation is further supported by movies of the temporal development of coherent structures (not shown).

VIII. Scalar Mixing

The consequences of the modifications of turbulence structures by swirl will be considered next. This will be done by considering the transport of a passive scalar (for example, the mixture fraction). Such investigations are relevant to turbulent combustion applications in which swirl is used to increase the burning intensity through enhanced mixing and a higher residence time [3].

The consequence of swirl effects for the turbulent mixing of passive scalars is illustrated in Fig. 14 that shows instantaneous scalar values in the centerplane $x_3 = 0$ and in the plane $x = 1D$, respectively. The $S = 0$ figure shows that the ordered ring structures have a relatively small effect on the scalar mixing: the mixing efficiency is relatively low. It is worth noting that the mixing in the near-nozzle exit region is not caused by molecular transport, but the mixing is driven by small-scale turbulence structures (the turbulent viscosity is about 20 times greater than the molecular viscosity in this region). The $S = 0.23$ figure shows that the modification of ring structures to helical and streamwise motions creates additional entrainment that enhances the turbulent mixing. The $S = 0.5$ figure shows that the breakup of helical structures further increases the turbulent mixing due to the random motion of the generated turbulent eddies. The $S = 0.75$ and $S = 1$ figures show that the large-scale turbulence structures observed in these flows lead again to an enhancement of turbulent scalar mixing. The bottom two centerplane contour plots (the $S = 0.75$ and $S = 1$ swirl cases) show that the jet plume has interacted with the far-field boundaries. This interaction may have a limiting effect on the spread of the jet plume, which means that the scalar transport results of the $S = 0.75$ and $S = 1$ swirl cases have to be taken with some caution. Nevertheless, there is convincing evidence that the increase of swirl obviously enhances the efficiency of turbulent scalar mixing for the range of swirl numbers considered.

A quantitative view of the mixing enhancement due to swirl is given by radial distributions of the scalar mean $\Phi = \langle\phi\rangle$ and scalar variance $\sigma_\phi^2 = \langle(\phi - \Phi)^2\rangle$, that are shown in Fig. 15. The $S = 0$ curves for the mean scalar Φ show the expected trend. The expansion of the jet with growing values x/D results in a development of the scalar profile from a step function at the nozzle exit toward the

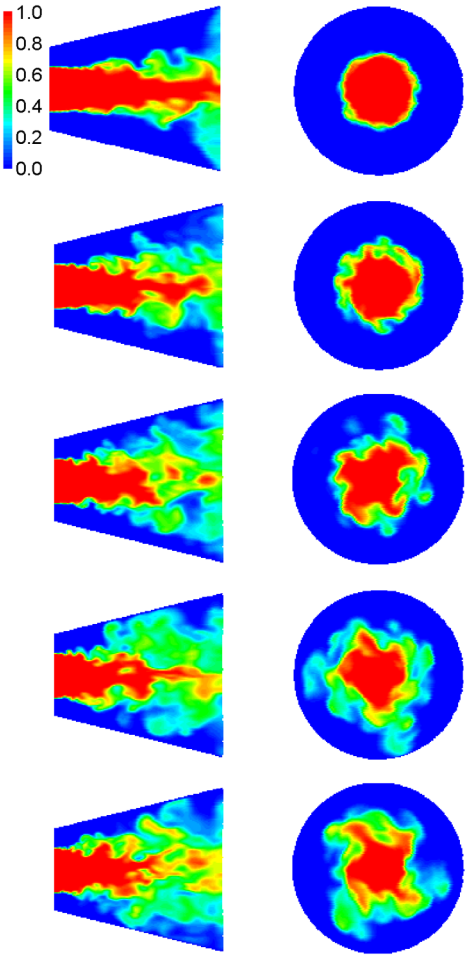

Fig. 14 Contour plots of instantaneous scalar values in the centerplane $x_3 = 0$ (left) and in the plane $x = 1D$ (right) for the swirl cases $S = 0, 0.23, 0.5, 0.75$, and 1 from the top to the bottom, respectively.

constant value $\Phi = 0.5$, corresponding to a complete mixing of the scalar. The mixing layer is characterized by the region with a maximum (and relatively constant) averaged scalar gradient centered at about $r/D = 0.5$. The scalar standard deviation σ_ϕ is approximately proportional to scalar gradients. Thus, the $S = 0$ curves of σ_ϕ show plateaulike high σ_ϕ values in the mixing layer region. The Φ and σ_ϕ curves for $1 \leq x/D \leq 3$ reveal that the addition of swirl leads to a significant reduction of scalar gradient values in the mixing layer and a related increase of the characteristic mixing layer thickness. For $x/D = 4$, the swirl effect becomes less relevant, because the scalar is

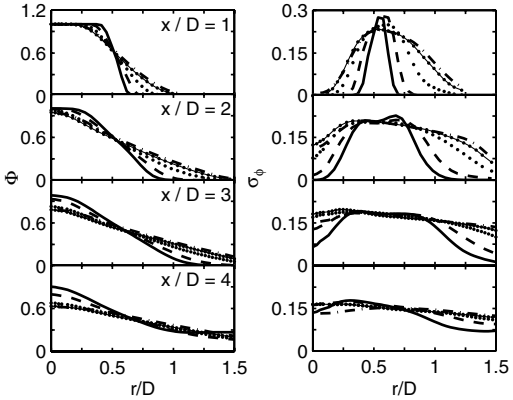

Fig. 15 Radial distributions of the mean scalar Φ and scalar standard deviation σ_ϕ at different axial positions x/D. Solid lines refer to the $S = 0$ case, dashed lines refer to the $S = 0.23$ case, dotted lines refer to the $S = 0.5$ case, solid lines with little dots refer to the $S = 0.75$ case, and dot-dashed lines refer to the $S = 1$ case.

already relatively well mixed at this axial position. For higher x/D values, one finds that the swirl effect becomes insignificant.

Obviously, a simple global conclusion regarding the mixing enhancement by swirl (one number which characterizes the mixing efficiency for each swirl case) would be very helpful. This question can be addressed by considering the intensity of segregation I, introduced by Danckwerts [34]:

$$I = \frac{\sigma_\phi^2}{\Phi(1-\Phi)} \tag{14}$$

According to its definition, the scalar variance can be written:

$$\sigma_\phi^2 = \langle \phi^2 \rangle - \Phi^2 = \Phi - \Phi^2 - \langle \phi(1-\phi) \rangle \tag{15}$$

By adopting the last expression in Eq. (14), one finds the following exact rewriting of the intensity of segregation:

$$I = 1 - \frac{\langle \phi(1-\phi) \rangle}{\Phi(1-\Phi)} \tag{16}$$

A closer look at expression (16) reveals the bounds for the intensity of segregation. A first case is given by a complete mixing. In this case, there are zero scalar fluctuations: this means the instantaneous scalar value ϕ is equal to the averaged scalar value Φ. In this case, the last term in Eq. (16) is equal to one, such that the intensity of segregation $I = 0$. A second case is given by a complete segregation. In this case, the instantaneous scalar value is either 1 or 0 at every point. Hence, the correlation between ϕ and $1-\phi$ must disappear ($\langle \phi(1-\phi) \rangle = 0$) because the product between ϕ and $1-\phi$ is always zero. Then, the last term in Eq. (16) disappears, such that the intensity of segregation $I = 1$. Correspondingly, the intensity of segregation I represents a convenient measure of the mixedness of a scalar that is bounded by zero and one ($0 \le I \le 1$), where $I = 0$ and $I = 1$ apply to the cases of a complete mixing and a complete segregation, respectively. The latter properties of the intensity of segregation suggest to define the mixing efficiency m_e by

$$m_e = 1 - I \tag{17}$$

The mixing efficiency (17) is bounded by zero and one ($0 \le m_e \le 1$). In particular, the value of the mixing efficiency m_e characterizes the amount of mixedness. The case $m_e = 0$ means that there is absolutely no mixing, and $m_e = 1$ means that the mixing is complete.

Figure 16 shows the mixing efficiency m_e for the different swirl cases considered. To have a global measure for the mixing intensity (one value which characterizes the amount of mixedness for each swirl case), the scalar values of one instant in time are used to calculate a scalar mean value and a scalar variance value as volume averages over all the computational domain. By adopting these values for the scalar mean and variance, the intensity of segregation (14) and the mixing efficiency (17) can be calculated for each swirl case considered. Figure 16 shows that the model function

$$m_e = 0.2 + \left[\frac{1.64S}{1 + 2.52S} \right]^2 \tag{18}$$

represents a very good approximation for the data values considered: the relative error magnitude of the approximation (18) is less than

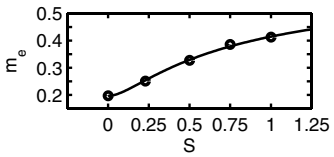

Fig. 16 The dependence of the mixing efficiency m_e on the swirl number S for the swirl cases considered. The dots give the results of Eq. (17), and the solid line represents the approximation (18) for the dependence of m_e on S.

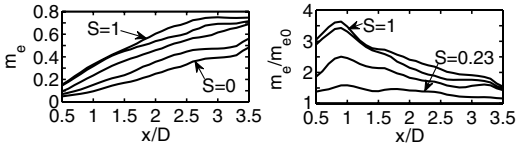

Fig. 17 The variation of the mixing efficiency m_e with the axial position x/D is shown for different swirl numbers S on the left-hand side. The bottom line refers to the $S = 0$ case. The m_e curves for the $S = 0.23$, $S = 0.5$, $S = 0.75$, and $S = 1$ cases are above the $S = 0$ curve, respectively. The mixing enhancement due to swirl is shown on the right-hand side by the ratio m_e/m_{e0}, where m_{e0} refers to the mixing efficiency of the $S = 0$ case. The ratio m_e/m_{e0} increases with the swirl number; this means the lowest curve corresponds to the $S = 0.23$ case, and the highest curve corresponds to the $S = 1$ case.

2%. It may be seen that the addition of swirl may significantly enhance the mixing intensity: the m_e difference between the $S = 1$ and $S = 0$ cases is given by 21.7%.

To get a better understanding of the spatial distribution of the mixing enhancement due to swirl, m_e is plotted as a function of the axial position x/D in Fig. 17 (left-hand-side plot). These m_e values are obtained at different axial positions x/D by averaging scalar values of one snapshot over a volume of width $1D$ centered at the axial position considered. The figure shows the expected trend of m_e variations: m_e increases, basically, linearly with x/D before it begins to level off. The addition of swirl enhances the mixing (the slope of the linear increase with x/D), such that m_e levels off at smaller x/D. The mixing enhancement due to swirl is quantified in terms of the right-hand-side plot of Fig. 17. This figure shows m_e normalized by the value m_{e0} for the $S = 0$ case. These curves reveal a maximum of m_e/m_{e0} close to $x/D = 1$. The reason for the appearance of this maximum is that the m_{e0} values for the $S = 0$ case do not increase much for $x/D < 1$. Hence, m_e/m_{e0} reflects (basically) the increase of m_e for the swirl cases in this region. For $x/D > 1$, the mixing efficiency m_{e0} of the $S = 0$ case shows a stronger increase than for $x/D < 1$ values, whereas the mixing efficiencies for the swirl cases begin to level off. Therefore, m_e/m_{e0} decreases for $x/D > 1$. The maximum value of m_e/m_{e0} shows the expected swirl dependence: the maximum value increases with the swirl number. The appearance of a maximum mixing enhancement may be relevant to applications of swirl to combustion chambers. The addition of swirl would significantly enhance the mixing close to the nozzle exit, which would result in a flame stabilization much closer to the nozzle exit (compared with the case without swirl). Hence, the length of the combustion chamber could be reduced.

IX. Conclusions

RANS and LES methods were combined to simulate swirling and nonswirling turbulent jet flows. In particular, RANS nozzle flow simulations were used to provide inlet profiles for the LES of jet flows. The RFG method of Smirnov et al. [14] was used for the generation of instantaneous LES inflow data. The advantage of this technique was given by the fact that it generated characteristic length and time scales of inflowing instantaneous turbulent eddies that were consistent with the corresponding RANS profiles imposed at the inlet. The comparison of averaged flowfields obtained by LES with the experimental data of Gilchrist and Naughton [17] revealed a good agreement. It was shown that the forcing applied clearly had a positive effect. Investigations of the suitability of various SGS closure models showed that the DSM and DKEM predict almost the same flowfields. The latter SGS models were found to provide better predictions than the SSM for the nonswirling case.

The validated LES method was used for studying swirling turbulent jet flows with swirl numbers S ranging from zero to one. The dynamics of coherent structures were studied in terms of an analysis of instantaneous flowfields provided by LES. In particular, instantaneous pressure fluctuation fields were found to be most appropriate for the visualization of coherent structures. This analysis revealed that swirl breaks apart the typical coherent ring structures of

nonswirling turbulent jet flows into two distinct structures: a helical mode and streamwise braid structures. The interaction of these structures generated unorganized turbulent motions that contributed to the enhancement of the turbulent mixing of scalars. The mixing efficiency $m_e = 1 - I$ was found to be an appropriate measure to quantify the amount of mixedness related to different swirl cases. It was shown that the analytical approximation (18) for the mixing efficiency m_e described the mixing enhancement due to swirl for the swirl number variations $0 \leq S \leq 1$ considered. It was shown that swirl could be used to increase the mixing efficiency by 21.7%. This fact was relevant, for example, to the optimization of turbulent combustion systems.

Acknowledgments

This work was sponsored by the U.S. Air Force Office of Scientific Research, under grant number FA9550-05-1-0485, monitored by John Schmisseur. The views and conclusions contained herein are those of the authors and should not be interpreted as necessarily representing the official policies or endorsements, either expressed or implied, of the U.S. Air Force Office of Scientific Research or the U.S. government. The computational resources have been provided by the Institute for Scientific Computation at the University of Wyoming. In particular, we would like to thank J. Naughton for his substantial support of our work. The view of the mechanism of swirl effects presented here is the result of many fruitful discussions with him. We are also thankful for his valuable suggestions for manuscript improvements. We would like to thank the referees for their very helpful suggestions for improvements.

References

[1] Farokhi, S., Taghavi, R., and Rice, E., "Modern Developments in Shear Flow Control with Swirl," *AIAA Journal*, Vol. 30, No. 6, 1992, pp. 1482–1483. doi:10.2514/3.11090

[2] Naughton, J. W., Cattafesta, L. N., and Settles, G., "An Experimental Study of Compressible Turbulent Mixing Enhancement in Swirling Jets," *Journal of Fluid Mechanics*, Vol. 330, 1997, pp. 271–305. doi:10.1017/S0022112096003679

[3] Syred, D. G., and Beer, J., "Combustion in Swirling Flows: A Review," *Combustion and Flame*, Vol. 23, No. 2, 1974, pp. 143–201. doi:10.1016/0010-2180(74)90057-1

[4] McIlwain, S., and Pollard, A., "Large Eddy Simulation of the Effects of Mild Swirl on the Near Field of a Round Free Jet," *Physics of Fluids*, Vol. 14, No. 2, 2002, pp. 653–661. doi:10.1063/1.1430734

[5] Garca-Villalba, M., and Fröhlich, J., "LES of a Free Annular Swirling Jet: Dependence of Coherent Structures on a Pilot Jet and the Level of Swirl," *International Journal of Heat and Fluid Flow*, Vol. 27, No. 5, 2006, pp. 911–923. doi:10.1016/j.ijheatfluidflow.2006.03.015

[6] Garcıa-Villalba, M., Fröhlich, J., and Rodi, W., "Identification and Analysis of Coherent Structures in the Near Field of a Turbulent Unconfined Annular Swirling Jet Using Large Eddy Simulation," *Physics of Fluids*, Vol. 18, No. 5, 2006, pp. 1–17. doi:10.1063/1.2202648

[7] Fröhlich, J., Garcıa-Villalba, M., and Rodi, W., "Scalar Mixing and Large-Scale Coherent Structures in a Turbulent Swirling Jet," *Flow, Turbulence and Combustion*, Vol. 80, No. 1, 2008, pp. 47–59. doi:10.1007/s10494-007-9121-3

[8] Shiri, A., George, W. K., and Naughton, J. W., "Experimental Study of the Far Field of Incompressible Swirling Jets," *AIAA Journal*, Vol. 46, No. 8, 2008, pp. 2002–2009. doi:10.2514/1.32954

[9] Vanierschot, M., and van den Bulck, E., "Influence of Swirl on the Initial Merging Zone of a Turbulent Annular Jet," *Physics of Fluids*, Vol. 20, No. 10, 2008, pp. 1–18. doi:10.1063/1.2992191

[10] Örlü, R., and Alfredsson, P. H., "An Experimental Study of the Near-Field Mixing Characteristics of a Swirling Jet," *Flow, Turbulence and Combustion*, Vol. 80, No. 3, 2008, pp. 323–350. doi:10.1007/s10494-007-9126-y

[11] Jakirlić, S., Hanjalić, K., and Tropea, C., "Modeling Rotating and Swirling Turbulent Flows: A Perpetual Challenge," *AIAA Journal*, Vol. 40, No. 10, 2002, pp. 1984–1996. doi:10.2514/2.1560

[12] Heinz, S., *Statistical Mechanics of Turbulent Flows*, Springer–Verlag, Berlin, 2003.

[13] Heinz, S., "Unified Turbulence Models for LES and RANS, FDF and PDF Simulations," *Theoretical and Computational Fluid Dynamics*, Vol. 21, No. 2, 2007, pp. 99–118. doi:10.1007/s00162-006-0036-8

[14] Smirnov, A., Shi, S., and Celik, I., "Random Flow Generation Technique for Large Eddy Simulations and Particle-Dynamics Modeling," *Journal of Fluids Engineering*, Vol. 123, No. 2, 2001, pp. 359–371. doi:10.1115/1.1369598

[15] Klein, M., Sadiki, A., and Janicka, J., "A Digital Filter Based Generation of Inflow Data for Spatially Developing Direct Numerical or Large Eddy Simulations," *Journal of Computational Physics*, Vol. 186, No. 2, 2003, pp. 652–665. doi:10.1016/S0021-9991(03)00090-1

[16] Bogey, C., and Bailly, C., "Effects of Inflow Conditions and Forcing on Subsonic Jet Flows and Noise," *AIAA Journal*, Vol. 43, No. 5, 2005, pp. 1000–1007. doi:10.2514/1.7465

[17] Gilchrist, R. T., and Naughton, J. W., "Experimental Study of Incompressible Jets with Different Initial Swirl Distributions: Mean Results," *AIAA Journal*, Vol. 43, No. 4, 2005, pp. 741–751. doi:10.2514/1.3295

[18] Stein, C. F., "Toward a Vortex Breakdown Condition for Swirling Annular Jets," *Journal of Fluids Engineering*, Vol. 121, No. 1, 1999, pp. 102–105. doi:10.1115/1.2821988

[19] Komori, S., and Ueda, H., "Turbulent Flow Structure in the Near Field of a Swirling Round Free Jet," *Physics of Fluids*, Vol. 28, No. 7, 1985, pp. 2075–2082. doi:10.1063/1.865388

[20] Schneider, C., Dreizler, A., and Janicka, J., "Fluid Dynamical Analysis of Atmospheric Reacting and Isothermal Swirling Flows," *Flow, Turbulence and Combustion*, Vol. 74, No. 1, 2005, pp. 103–127. doi:10.1007/s10494-005-7369-z

[21] Menter, F. R., "Two-Equation Eddy-Viscosity Turbulence Models for Engineering Applications," *AIAA Journal*, Vol. 32, No. 8, 1994, pp. 1598–1605. doi:10.2514/3.12149

[22] *FLUENT 6.3 User Guide*, FLUENT, Inc., Lebanon, NH, 2006.

[23] Heinz, S., and Roekaerts, D., "Reynolds Number Effects on Mixing and Reaction in a Turbulent Pipe Flow," *Chemical Engineering Science*, Vol. 56, No. 10, 2001, pp. 3197–3210. doi:10.1016/S0009-2509(00)00539-X

[24] Mathey, F., Cokljat, D., Bertoglio, J. P., and Sergent, E., "Assessment of the Vortex Method for Large Eddy Simulation Inlet Conditions," *Progress in Computational Fluid Dynamics*, Vol. 6, Nos. 1–3, 2006, pp. 58–67. doi:10.1504/PCFD.2006.009483

[25] Kraichnan, R., "Diffusion by a Random Velocity Field," *Physics of Fluids*, Vol. 13, No. 1, 1970, pp. 245–272. doi:10.1063/1.1692799

[26] Glaze, D. J., and Frankel, S. H., "Stochastic Inlet Conditions for Large-Eddy Simulation of a Fully Turbulent Jet," *AIAA Journal*, Vol. 41, No. 6, 2003, pp. 1064–1073. doi:10.2514/2.2073

[27] Pope, S. B., *Turbulent Flows*, Cambridge Univ. Press, Cambridge, England, U.K., 2000.

[28] Smagorinsky, J., "General Circulation Experiments with the Primitive Equations, 1: The Basic Experiment," *Monthly Weather Review*, Vol. 91, No. 3, 1963, pp. 99–164. doi:10.1175/1520-0493(1963)091<0099:GCEWTP>2.3.CO;2

[29] Germano, M., Piomelli, U., Moin, P., and Cabot, W. H., "A Dynamic Subgrid-Scale Eddy Viscosity Model," *Physics of Fluids*, Vol. 3, No. 7, 1991, pp. 1760–1765. doi:10.1063/1.857955

[30] Kim, W.-W., and Menon, S., "Application of the Localized Dynamic Subgrid-Scale Model to Turbulent Wall-Bounded Flows," AIAA Paper 97-0210, 1997.

[31] Escudier, M. P., and Keller, J. J., "Recirculation in Swirling Flow: A Manifestation of Vortex Breakdown," *AIAA Journal*, Vol. 23, No. 1, 1985, pp. 111–116. doi:10.2514/3.8878

[32] Sarpkaya, T., "Vortex Breakdown in Swirling Conical Flows," *AIAA*

Journal, Vol. 9, No. 9, 1971, pp. 1792–1799.
doi:10.2514/3.49981

[33] Loiseleux, T., Chomaz, J. M., and Huerre, P., "The Effect of Swirl on Jets and Wakes: Linear Instability of the Rankine Vortex with Axial Flow," *Physics of Fluids*, Vol. 10, No. 5, 1998, pp. 1120–1134.
doi:10.1063/1.869637

[34] Danckwerts, P. V., "The Definition and Measurement of Some Characteristics of Mixtures," *Applied Scientific Research, Section A*, Vol. 3, No. 4, 1952, pp. 279–296.

P. Givi
Associate Editor